crystals

MDPI

Review

Emerging Perovskite Nanocrystals-Enhanced Solid-State Lighting and Liquid-Crystal Displays

Ziqian He [1], Caicai Zhang [2,3], Yajie Dong [1,2,3] and Shin-Tson Wu [1,*]

[1] College of Optics and Photonics, University of Central Florida, Orlando, FL 32816, USA; zhe@knights.ucf.edu (Z.H.); Yajie.Dong@ucf.edu (Y.D.)
[2] Department of Materials Science & Engineering, University of Central Florida, Orlando, FL 32816, USA; cczhang@knights.ucf.edu
[3] NanoScience Technology Center, University of Central Florida, Orlando, FL 32826, USA
* Correspondence: swu@creol.ucf.edu

Received: 11 January 2019; Accepted: 20 January 2019; Published: 22 January 2019

Abstract: Recent advances in perovskite nanocrystals-enhanced solid-state lighting (SSL) and liquid-crystal displays (LCDs) are reviewed. We first discuss the development, optical properties, and stability issue of materials, and then we evaluate the performance of SSL and LCDs with perovskite downconverters adopted. In SSL performance evaluation, we investigate the fitting-curve effect in calculations and optimizations where simple Gaussian fitting and precise fitting are compared in detail, and we further optimize for highly efficient, good color-rendering, and human-healthy SSL sources. For LCD performance evaluation, we study the intrinsic tradeoffs between total light efficiency and color gamut coverage. Through optimizations using real line shapes, Rec. 2020 standard coverage as large as 92.8% can be achieved through hybrid integration. Finally, we briefly discuss two future challenges: materials development and device integration. We believe the emerging perovskite nanocrystals are highly promising for next-generation SSL and LCDs.

Keywords: perovskite nanocrystals; photoluminescence; solid-state lighting; color quality scale; circadian effect; liquid-crystal displays; wide color gamut

1. Introduction

Since the invention of high-performance blue light-emitting diodes (LEDs) [1–3], phosphor-converted white LED (pc-WLED) has found widespread applications, especially in solid-state lighting (SSL) and liquid-crystal display (LCD) backlight, due to its high efficiency, long lifetime, low cost, simple optical configuration, high brightness, and fast response time [4–6]. The huge market share and still-growing needs promote the studies further. During the past decades, SSL researches have been focusing on pushing the efficiency [7–9]. However, SSL aiming at beyond energy saving, such as human healthy lighting or horticultural lighting, becomes more and more important and starts to gain attention [10,11]. Thus, the ability to tailoring spectral power distribution (SPD) of emitters according to specific requirements while keeping high efficiency is pivotal. Meanwhile, the request for large color gamut LCDs also becomes urgent. As the color gamut evaluation metric gradually upgraded from sRGB (standard Red Green Blue), via NTSC (National Television Standards Committee), and now to Rec. 2020, the traditional pc-WLED cannot fulfill the demand for highly vivid colors [12–14]. Emitters that can accomplish the requirements by next-generation SSL and LCD backlight are thus highly desirable.

In the past few years, organic-inorganic hybrid and all-inorganic halide perovskites have been explored intensively, as they are promising in applications, such as photovoltaic, LED, photodetectors, and transistors [15–22]. Moreover, their excellent photoluminescent properties make them a strong

contender for next-generation SSL and LCD backlight. As downconverters, they are not only color-tunable and narrow-band, but also easy-to-synthesize and low-cost. These properties can potentially fulfill the SSL's requirements, including high efficiency and capability of tailoring the SPD. Also, the narrow-band emission ensures vivid colors, which are essential for large color gamut LCDs.

In this review, we summarize recent advances of perovskite downconverter-enabled high-performance SSL and LCD backlight. In Section 2, we begin with a brief description of the materials development and characterization. In Section 3, we evaluate the adoption of perovskite downconverters for efficient, good color-rendering, healthy, tunable SSL, with first discussing the fitting-curve effect in SSL. In Section 4, we discuss the systems performance of LCDs that apply perovskite downconverters for large color gamut and high efficiency. Finally, in Section 5, two future challenges are emphasized: materials development and device integration.

2. Materials Development and Characterization

Metal halide perovskites (MHPs) have a most general chemical formula of ABX_3, where A represents cations, such as Cs^+, $CH_3NH_3^+$, or $CH(NH_2)^{2+}$, B relates to metal cations usually as Pb^{2+}, and X is halide anion like Cl^-, Br^-, or I^- [23,24]. In their crystalline structures, B cation coordinates with six halide anions to form a corner-shared [BX_6] octahedral configuration with A cation located in each large void between the octahedra, so that to form cubic or orthorhombic structures [25,26].

Currently, lead halide perovskite nanocrystals (PNCs) are the most promising candidates that can replace phosphors or quantum-dots (QDs) in SSL and LCD backlight [27–31]. These PNCs exhibit large freedom of tailoring emission peaks. Their emission peak wavelength can be easily tuned through halide composition variations. For example, $CsPbBr_3$ NCs with size larger than 11 nm shows a photoluminescence (PL) peak at around 520 nm [32]. Adjusting the chemical composition to $CsPbCl_xBr_{3-x}$ and $CsPbBr_xI_{3-x}$ will shift the emission peak to shorter and longer wavelengths, respectively, and the entire visible band can be covered. Another intriguing optical property is their excellent color purity. The emission line widths in visible band are narrow, and the full widths at half maximum (FWHM) of PNCs are usually in the range of 12–40 nm. When integrated in SSL or LCD backlight, a blue LED is often applied as the pumping source. Figure 1 depicts the 450-nm blue LED-excited PL spectra of representative lead halide PNC series with varying halide compositions. A typical trend is that shorter emission peak wavelength exhibits a narrower FWHM. Besides these two properties, PNCs can also achieve a high PL quantum yield, even higher than 90% [33].

Generally, there are two kinds of methods to synthesize PNCs. In 2015, Kovenlenko et al. reported a strategy to synthesize all-inorganic ($CsPbX_3$) PNCs by mixing Cs-oleate and PbX_2 precursors in octadecene with ligands, and precipitate PNCs at high temperature. This strategy is very similar to the traditional hot-injection method for QD synthesis [33]. In the same year, Zhong et al. introduced another method, termed the ligand-assisted reprecipitation (LARP) technique, where the perovskite precursors were simply dropped into poor solvent to form PNCs [34]. By changing the composition of the cations or halide anions X, both methods can help to produce PNCs with great color tunability, excellent luminescent efficiency, and ultrahigh color purity [35–40].

However, PNCs that were fabricated through above-mentioned methods suffer from poor stability. PNCs that are easy to be formed are easy to be decomposed as well because of the low formation energy [41–43]. Water, heat, light, oxygen, or combing effects in the ambient air will all accelerate the decomposition of the perovskite nanoparticles and further lead to the luminescent quenching [44,45]. Therefore, strategies, such as using zwitterionic ligand, encapsulating PNCs into inert shells, and in-situ synthesis of perovskite nanoparticles in or on a polymer or inorganic matrix have been developed [26,46–50]. Among them, in-situ fabrication becomes more and more predominant, since it holds great promise on the stabilization of the embedded PNCs in target device structures [51–53]. For instance, a controlled drying in-situ method has already been used by Zhijing Nanotech and Lucky Cooperation in the fabrication of the first perovskite QD-embedded composite film (PQDCF)-based wide color gamut LCD prototype [51].

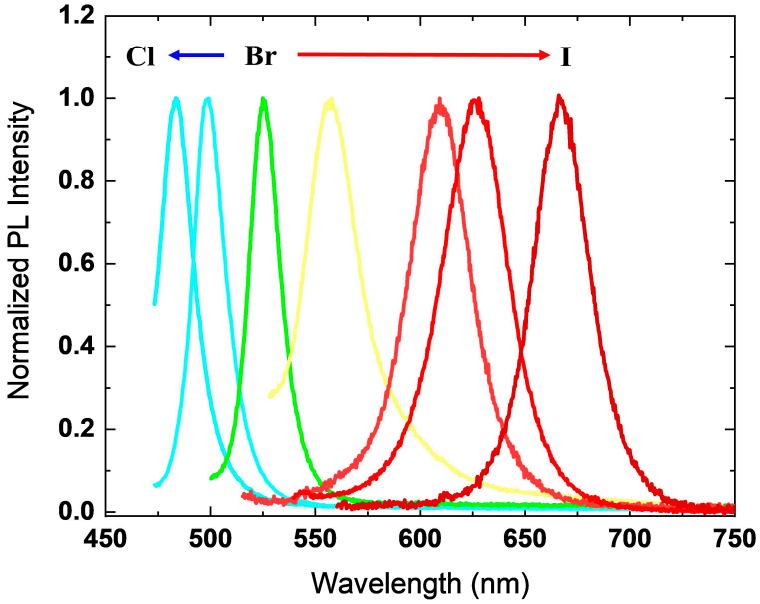

Figure 1. Photoluminescence (PL) spectra of a series of perovskite nanocrystals (PNCs) with different halide compositions under a 450-nm blue light-emitting diodes (LED) excitation.

Beside the stability issue of PNCs, the presence of lead remains to be a concern for these materials to be widely used in consumer electronics. Efforts have been devoted to finding the environmentally friendly elements in the perovskite structure to replace lead, such as Sn^{2+} and Ge^{2+} [54–56]. However, at the current stage, the as-synthesized particles are either highly unstable and are sacrificed from degradation after only a few hours [57], or of relatively poor color purity not comparable with lead halide perovskites [56,58].

3. Solid-State Lighting Applications

The past decades have witnessed the thriving of SSL. It outperforms incandescent and fluorescent light bulbs in many aspects, such as power consumption, lifetime, size, brightness, and response time. The discovery and synthesis of new downconverters, such as phosphors [59–61] and QDs [62,63], keep promoting the performance of SSL so that SSL starts to aim at beyond energy saving. Previously, some studies have been focusing on perovskite-enabled high-performance SSL [64–67]. Here, we discuss the adoption of these new downconverters into RG_pB (Red, blue LED chips plus green perovskite downconverters) and RY_pG_pB (Red, blue LED chips plus yellow, green perovskite downconverters) type SSL for achieving highly efficient, excellent color-rendering, healthy, tunable lighting. These combinations allow independent intensity tuning of each color and avoid the green gap of LEDs [68].

At very early stages, numerous researches have been devoted to optimizing SSL's energy efficiency and color rendering performance [69–74]. However, as the biological impacts of light have been studied extensively [75–79], researches started to take human-health effect into SSL design [80–83]. Under ambient light, the intrinsically photosensitive retinal ganglion cells (ipRGCs) innervating the suprachiasmatic nucleus (SCN) can influence the melatonin secretion, and thus affect the circadian rhythm [84]. In reference to the experiments on light-induced melatonin suppression, the action spectrum of the circadian effect with a peak at blue wavelength was proposed [85,86]. Lately, studies, optimizations, and designs of SSL that take circadian effect into consideration were emerging rapidly. Meanwhile, the color quality metrics of SSL are also advancing [87]. To overcome the deficits of outdated color rendering index (CRI), many metrics are proposed, such as color quality scale (CQS), color fidelity index (CFI), color gamut index (CGI), etc. For example, CQS is calculated using 15 Munsell test color samples and it is more suitable for artificial light sources that enhance the object chroma.

Recently, plethora of studies started to apply different rendering quality metrics instead of CRI. In this review, we follow their steps and take one step further to investigate the intrinsic tradeoffs among luminous efficacy of radiation (LER), CQS, and circadian action factor (CAF) for these two types of SSL. LER is a measure of light spectral efficiency, defined as:

$$LER = \frac{K_m \int S(\lambda)V(\lambda)d\lambda}{\int S(\lambda)d\lambda}, \quad (1)$$

where K_m = 683 lm/W is the LER of ideal monochromatic 555-nm source, $S(\lambda)$ the SPD of the white light, and V(λ) the human eye sensitivity function. CQS, as the measure of color rendering quality, is calculated following [88]. CAF characterizes the circadian effect of light, which can be quantified by:

$$CAF = \frac{K_c \int S(\lambda)C(\lambda)d\lambda}{\int S(\lambda)V(\lambda)d\lambda}, \quad (2)$$

where $C(\lambda)$ is the circadian action function [85] and K_c is a normalization constant that ensures CAF = 1 for the International Commission on Illumination (CIE) standard daylight illuminant D65. In our optimization, five correlated color temperatures (CCTs), including 2700K, 3500K, 4500K, 5500 K, and 6500K are taken into consideration for tunable lighting sources. The objectives are:

$$aLER = \frac{1}{5}\sum_{i=1}^{i} LER_i, \quad (3)$$

$$aCQS = \sqrt{\frac{1}{5}\sum_{i=1}^{i} CQS_i^2}, \quad (4)$$

$$vCAF = \frac{CAF_5}{CAF_1}, \quad (5)$$

where i (i = 1 ~ 5) refers to each CCT (from 2700K to 6500K) and the root mean square value of aCQS is employed to avoid large discrepancies between different CCTs. Besides defining the objectives, it is also necessary to specify that the central wavelengths of emitters are limited in variant ranges according to their colors and the bandwidths of red and blue LEDs are set to 20 nm, while the bandwidths of green and yellow perovskite downconverters can be varied from 17 to 25 nm.

During the optimization, four optimization algorithms (genetic algorithm, particle swarm optimization, differential evolution, and adaptive simulated annealing) are utilized interchangeably to obtain global optimal solutions. For multi-objective optimizations, the intrinsic tradeoffs among objectives will create a unique geometry, termed *Pareto Front* [89], where each individual on the geometry demonstrate an optimal solution that has at least one objective outperforming that of others.

3.1. Fitting-Curve Effect

Before evaluating device performance, the effect of using fitting curves for replacing real SPDs in optimizations is worth discussing. Many fitting models have been proposed and applied in optimizations [90–93]. Among them, the Gaussian fitting in wavelength scale is the simplest. When compared with it, real SPDs are usually not symmetric and decrease more slowly when deviating from the emission peak wavelength. The utilization of fitting functions can simplify the data acquisition and lead to more general results. However, a natural question, how accurate the optimization results are when fitting curves are employed, needs to be addressed. To analyze this question, we evaluate the performance of optimized SSL for both RG_pB and RY_pG_pB types at a fixed CCT (2700 K), where LER, CQS, and CAF are the three objectives. Typically, low CCT SSL sources are suitable for evening lighting, where high LER and CQS with low CAF are preferred. To make a comparison, we chose Gaussian

function (Equation (6)) and Split-Pearson VII function (SP7, Equation (7)) [93] for simple fitting and precise fitting, respectively:

$$S_G(\lambda, \lambda_0, \Delta\lambda) = e^{-4\ln 2\frac{(\lambda-\lambda_0)}{\Delta\lambda^2}}, \tag{6}$$

$$\begin{aligned} S_{SP7}(\lambda, \lambda_0, \Delta\lambda) &= \frac{1}{\left[1+\left(\frac{\lambda-\lambda_0}{a}\right)^2\left(2^{\frac{1}{b}}-1\right)\right]^b}(\lambda < \lambda_0); \\ &= \frac{1}{\left[1+\left(\frac{\lambda-\lambda_0}{\Delta\lambda-a}\right)^2\left(2^{\frac{1}{c}}-1\right)\right]^c}(\lambda \geq \lambda_0), \end{aligned} \tag{7}$$

where λ_0 is the emission peak wavelength, $\Delta\lambda$ the FWHM, and a, b, c the fitting parameters. SPDs of blue LED, green perovskite, and red LED using these two models are presented in Figure 2 and the fitting parameters a, b, and c are listed in Table 1. In comparison with ideal Gaussian functions, the realistic SPDs are not symmetric on both sides of the emission peak wavelength and show longer "tails".

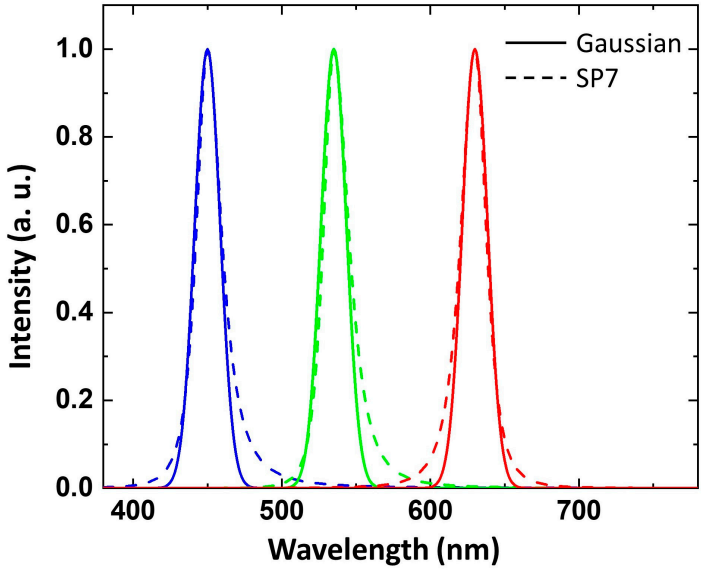

Figure 2. Spectral power distribution (SPDs) of blue LED, green perovskite-polymer downconverter, and red LED. The solid lines denote Gaussian fitting model and the dashed lines are based on precise fitting (SP7) model.

Table 1. Fitting parameters in SP7 model of all variable SPDs.

	a (nm)	b	c	$\Delta\lambda$ (nm)
Blue LED	8.7579	1.8468	1.3060	18.3
Green Perovskite	8.1711	2.3090	1.5763	18.4
Red LED	11.0988	1.8285	1.8049	17.3
Red QD	11.1176	1.9608	2.2252	22.8

The *Pareto Fronts* of optimized SSL for RG_PB and RY_PG_PB types at a fixed CCT (2700K) is plotted in Figure 3a–c and 3d–f as three-view diagrams, respectively. When compared with the SP7 model, the Gaussian model can achieve lower minimum CAF and larger maximum LER when CQS is low, but the highest-achievable CQS is sacrificed. However, if we focus on the moderate CQS range for RG_PB type and the relatively high CQS range for RY_PG_PB type, the performance of the optimized SSL is comparable. Nevertheless, when comparing the *Pareto Fronts* obtained by applying these two fitting models is not enough. If they exhibit similar performance but dramatically different emission peak wavelengths, the simplified model still cannot present the practical cases and provide useful information. To clarify, the correlations between the emission peak wavelengths and the objectives of

these two types SSL are illustrated in Figures 4 and 5, respectively. Both models show very similar emission peak preference and trend. By the above analysis, optimizations using the simplified model indeed provide useful information, so that we can adopt Gaussian model into our simulation in the next sub-section.

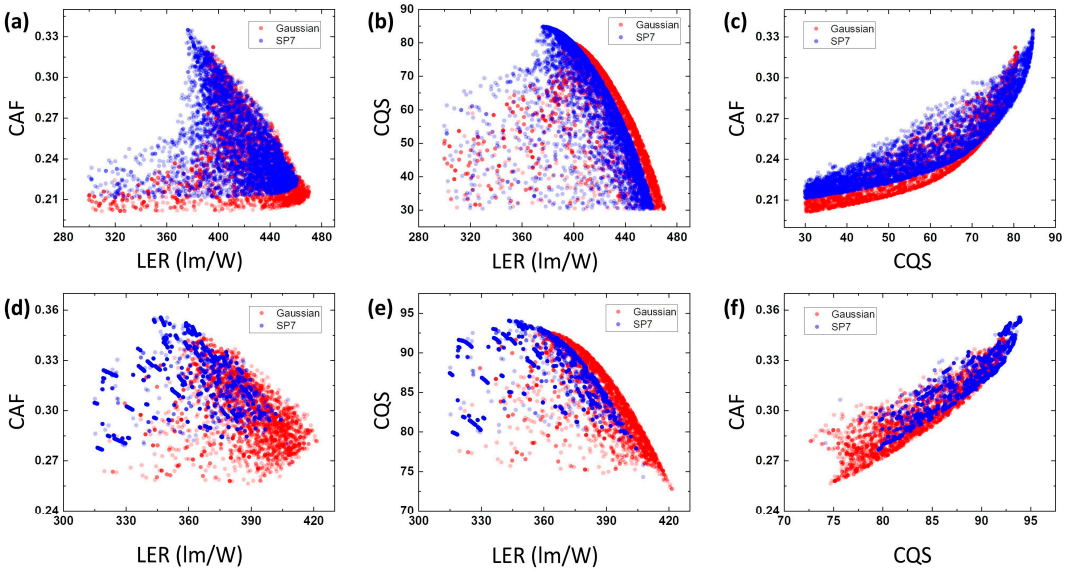

Figure 3. *Pareto Fronts* in three-view diagrams of optimized (**a**–**c**) RG_PB- and (**d**–**f**) RY_PG_PB-type solid-state lighting (SSL) at a fixed correlated color temperature (CCT) (2700K). Both Gaussian and SP7 model are calculated for comparison.

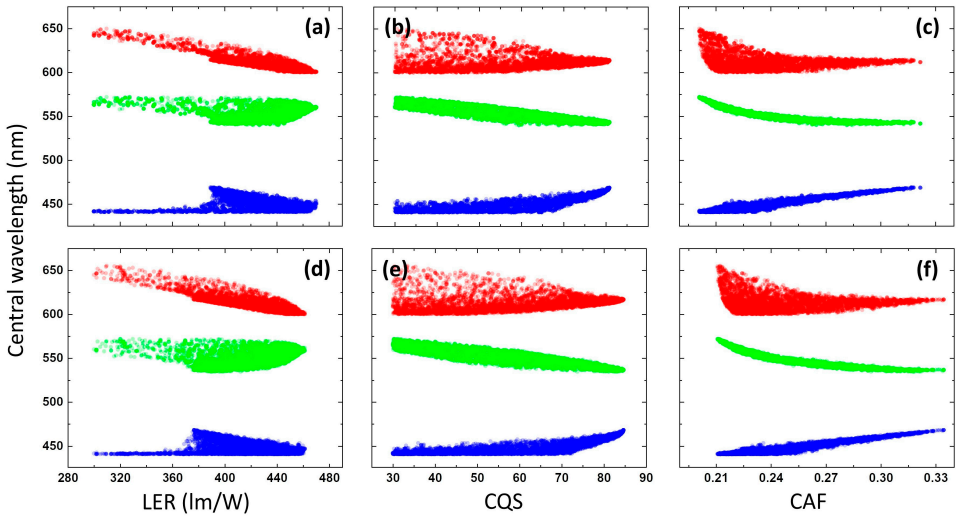

Figure 4. Correlations between the emission peak wavelengths and the objectives for optimized RG_PB-type SSL, where (**a**–**c**) Gaussian model and (**d**–**f**) SP7 model are applied in the optimization.

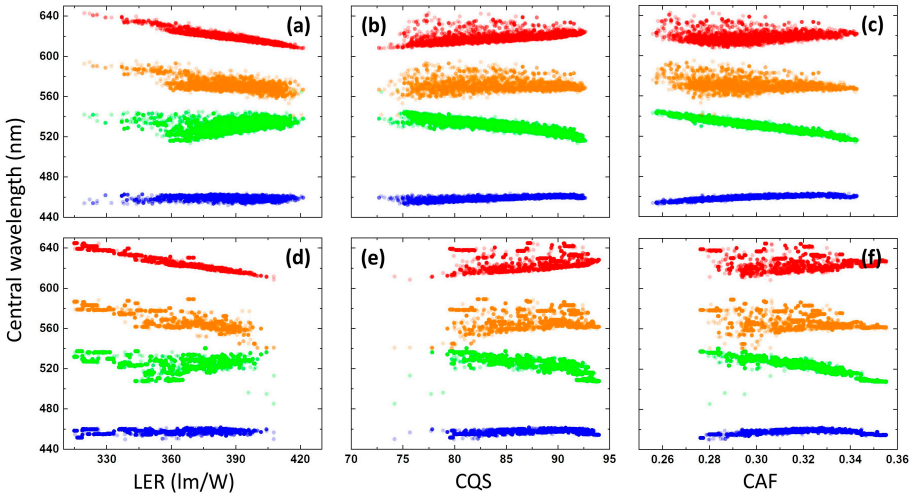

Figure 5. Correlations between the emission peak wavelengths and the objectives for optimized RY_PG_PB-type SSL, where (**a**–**c**) Gaussian model and (**d**–**f**) SP7 model are applied in the optimization.

3.2. Device Performance

The three-view diagrams of *Pareto Front* for RG_pB and RY_pG_pB types are depicted in Figures 6 and 7, respectively. The geometries for these two types are distinct. For the RG_pB type, vCAF is constrained by the other two objectives on both upper and lower limits, while aCQS and aLER are mutual exclusive on the upper limit. This differs from the RY_pG_pB type, in that the objectives for such a type are mutual exclusive only on the upper limit when the lowest vCAF is similar for both types. By adding one more emitter, the RY_pG_pB type SSL can achieve about 94 aCQS and 4.7 vCAF, while RG_pB type can merely accomplish around 80 aCQS and 3.4 vCAF. The improvement of aCQS (17.5%) and vCAF (38.2%) is large when compared to the RG_pB type.

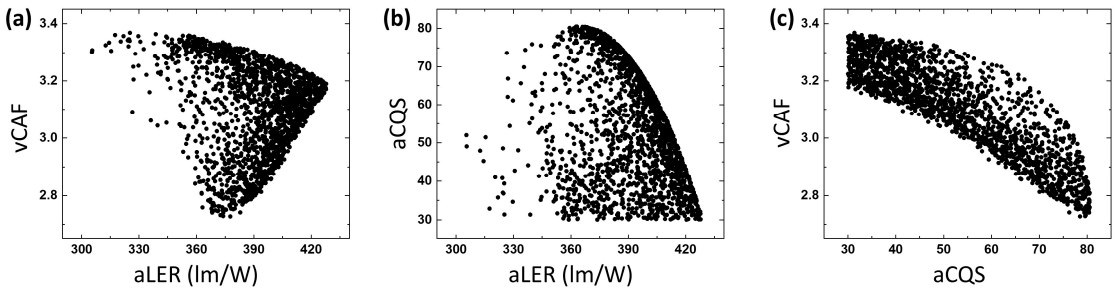

Figure 6. *Pareto Fronts* in three-view diagrams of optimized (**a**–**c**) RG_PB-type SSL where CCT varies from 2700K to 6500K.

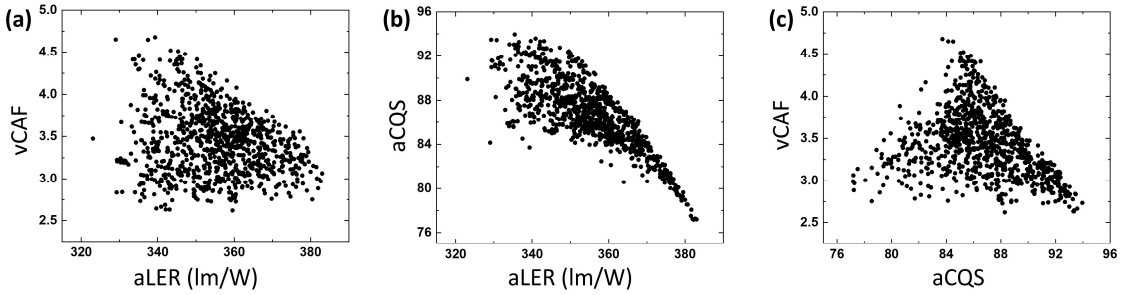

Figure 7. *Pareto Fronts* in three-view diagrams of optimized (**a**–**c**) RY_PG_PB-type SSL where CCT varies from 2700K to 6500K.

One optimal solution per each type is chosen for further detailed studies. The SPDs of RG_pB- and RY_pG_pB-type optimal solutions are illustrated in Figure 8a,b, respectively. RG_pB type offers

333.8 lm/W aLER, 65.6 aCQS, and 3.22 vCAF, while RY_pG_pB type provides 333.0 lm/W aLER, 87.1 aCQS, and 3.88 vCAF. With similar aLER, RY_pG_pB shows 32.8% higher aCQS and 20.5% higher vCAF than RG_pB. Their LER, CQS, and CAF values as a function of CCT are demonstrated in Figure 8c, where those values of reference white (blackbody radiator at CCT< 5000K and CIE standard illuminant at CCT$\geq$ 5000K) are also presented. The two optimal solutions have similar luminance efficacy, while the color rendering quality of RY_pG_pB type outperforms the RG_pB type, especially at higher CCTs. Moreover, RY_pG_pB type can follow the circadian phase of reference white better and provide much wider tuning at both high and low CCTs. Through the analysis, we see that the RY_pG_pB-type optimal solution is indeed a highly efficient, good color-rendering, and human-healthy SSL source.

Noticed in Figure 8a, the gaps between different bands are so large that RG_pB type is hard to achieve good color rendition (CQS metric). Under this circumstance, narrow-band emitters may not be a good choice. However, adding another emitter (RY_pG_pB) improves the overall performance significantly. Further increasing the number of emitters (e.g. $RY_pG_pC_pB$) should achieve even better performance. Yet, in practice, the number of independently tunable emitters will tradeoff with the complexities of driving circuits and color-mixing optics design. Therefore, the four emitters-type SSL sources should be a good choice with both moderate design complexities and high overall system performance.

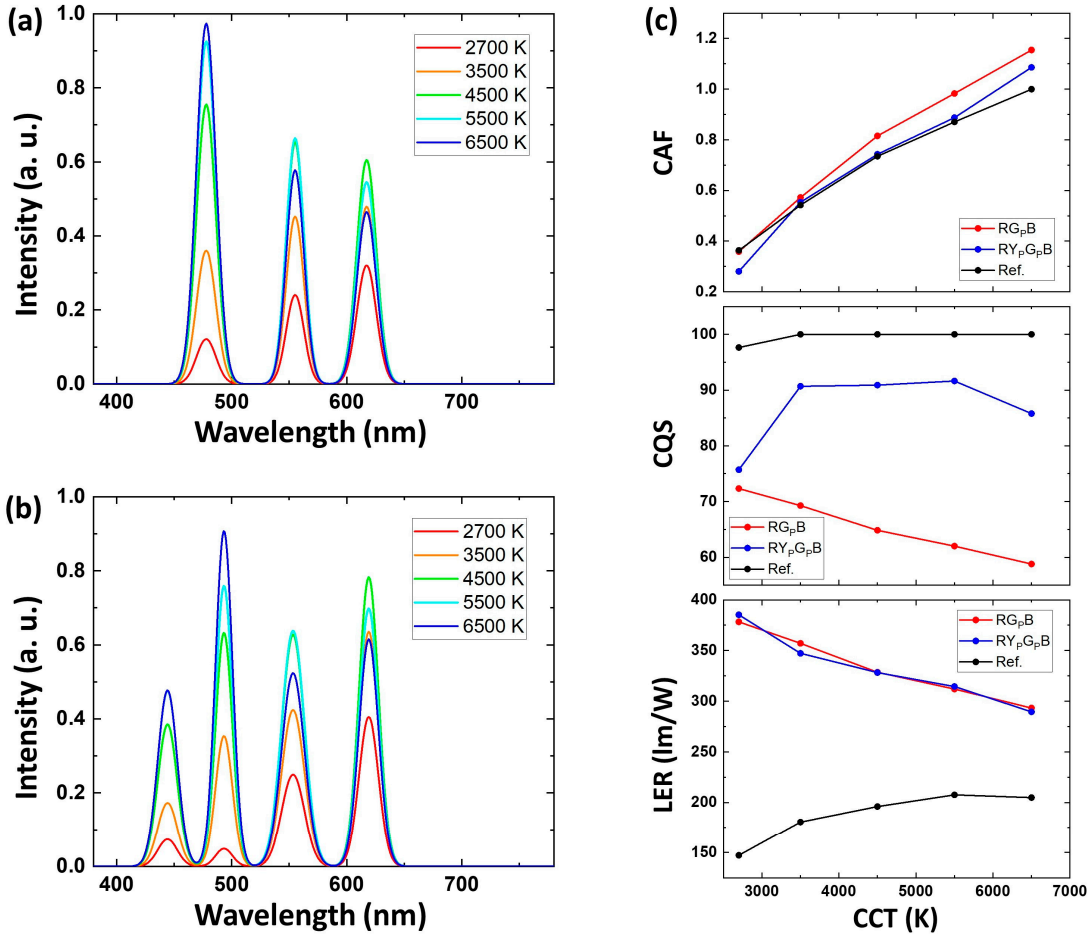

Figure 8. SPDs of individual optimal solution at different CCTs for (**a**) RG_PB (peak wavelengths: 477.9 nm, 555.1 nm and 617.3 nm) and (**b**) RY_PG_PB (peak wavelengths: 444.2 nm, 493.3 nm, 553.3 nm, and 619.1 nm) type SSL. (**c**) The detailed performance as a function of CCT.

4. LCD Backlight Applications

Another important application of perovskite downconverters is LCD backlight. As an essential part of LCDs, designs of backlight influence the color gamut, optical efficiency, viewing angle, and so on [94–96]. Currently, phosphor-converted white LEDs are the mainstream of LCD backlight [97,98]. They show relatively high efficiency, long lifetime, low cost, and simple optical configuration. However, as the color-gamut evaluation metrics keep advancing, the development of novel narrow-band emitters becomes increasingly crucial. The recently developed stable, narrow-band (18 nm), low cost, easy-to-synthesize green perovskite-polymer films have proven to be a promising candidate for wide color gamut LCDs [99]. However, stable and narrow-band red downconverters are still missing. Thus, hybrid backlight systems are preferred. Figure 9 depicts the schematic diagrams for three hybrid backlight systems. Detailed operation mechanisms will be discussed, as follows.

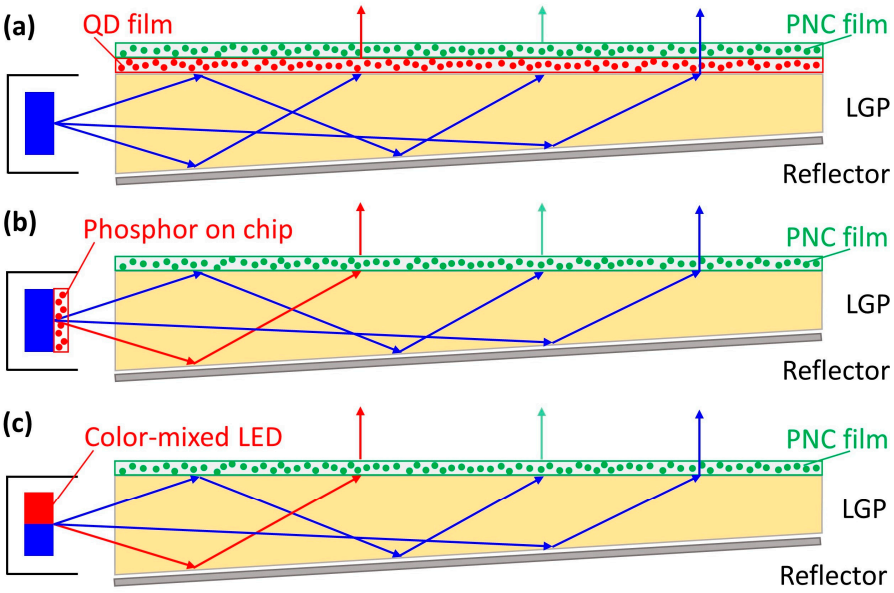

Figure 9. Schematic diagram for three different hybrid configurations implementing on-surface PNC films with (**a**) on-surface red quantum-dots (QD) film; (**b**) on-chip red phosphor; (**c**) color-mixed LED chips.

Figure 9a utilizes on-surface green perovskite-polymer and red QD films. Currently, the emission spectra of QD enhancement film (QDEF) still have around 30-nm FWHM at green color and the on-surface approach needs a large amount of QDs [100]. This approach results in a moderate highest-achievable Rec. 2020 standard coverage of around 82% and the QDEF itself is still expensive [101]. The hybrid on-surface configuration can enlarge the color gamut, lower the cost, and ensure that the working temperature is around room temperature, which helps to enhance the reliability and long-term stability of both QDs and perovskite nanocrystals significantly. However, since a large amount of red QDs are still needed, this approach is only suitable for high-end LCDs at this stage. Figure 9b shows another configuration where red phosphor (KSF or others) on-chip is applied instead of the on-surface red QD films, due to phosphors' high quantum efficiency and good high-temperature stability. Compared to the two phosphor-converted WLED (2pc-WLED) approach, this hybrid method can greatly enlarge the color gamut, since the green phosphors with ideal emission peak wavelength are still quite broadband (FWHM ~ 50 nm), such that the color crosstalk of the color filters (CFs) will deteriorate the ultimate performance [102,103]. Figure 9c demonstrates another possibility that employs color-mixed LED chips. When comparing to RGB-LED backlight [104–106], this approach utilizes high-performance LEDs and avoids the green gap. Moreover, it saves the down-converting photon energies that are otherwise costed by red phosphors. However, the adoption

of this approach needs to overcome some potential technical challenges such as light guide plate design, color-mixing issue, and thermal effects on LED chips, etc.

Previously, device performance of some hybrid systems has been investigated in a discrete sense, i.e., with fixed peak emission wavelengths. In their calculation, 91.6% of Rec. 2020 standard coverage can be achieved by hybridizing green perovskite-polymer downconverters with red QDs whose emission peak wavelength is at 650 nm [99]. Here, by assuming that the line shapes of tunable emitters keep unchanged within a small range of peak emission wavelengths, a more thorough study can be accomplished and the ultimate tradeoffs between color gamut coverage (CGC) and total light efficiency (TLE) can be evaluated.

For a typical LCD panel, the backlight will pass through three channels: red (R), green (G), and blue (B). Each channel will be sequentially modulated by the polarizer, LC, analyzer, and corresponding CF. The final output light from these three sub-pixels is then mixed to form a color pixel. Following the steps in [107,108] and assuming that the pixel displays reference white (CIE standard illuminant D65), we calculate the *Pareto Front* of the two-objective (CGC and TLE) optimization. Here, CGC is defined as the intersection between display color gamut area and standard color gamut area, which in our case is Rec. 2020:

$$CGC = \frac{A_{display} \cap A_{standard}}{A_{standard}}. \tag{8}$$

TLE is calculated, as follows:

$$TLE = \frac{K_m \int S_{out}(\lambda) V(\lambda) d\lambda}{\int S_{in}(\lambda) V(\lambda) d\lambda}, \tag{9}$$

where S_{in} is the SPD of backlight and S_{out} the SPD of final output light from the pixel. Note that CGC in different color spaces is not the same. A previous discussion suggested that CGC in CIE 1931 color space is more correlated to the three-dimensional (3D) color perspective model [109]. Under this consideration, we calculate CGC in CIE 1931. Meanwhile, different LC modes exhibit almost the same *Pareto Front* geometry and highest achievable CGC but only differ in TLE [109]. Therefore, here we use in-plane switching (IPS) mode as an example. Two sets of commercial CFs are considered: one with higher transmittance but larger crosstalk and the other with the opposite, as depicted in Figure 10a.

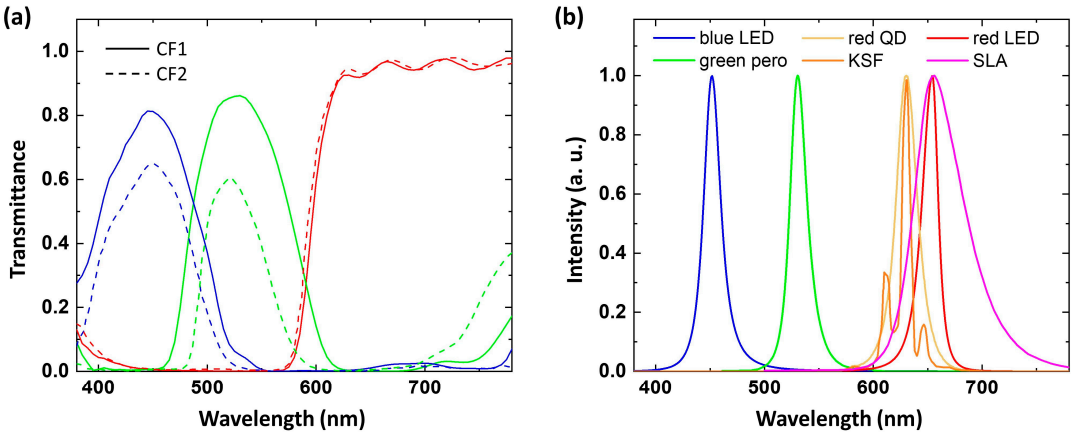

Figure 10. (**a**) Transmission spectra of two commercial color filters. (**b**) Spectra of RGB primaries used in optimizations.

Because Gaussian fitting introduces a relatively large deviation on the results [101], we employ SP7 as a more precise fitting model. To specify, four combinations are investigated: RG_PB (red, blue LEDs plus green perovskite), R_QG_PB (blue LED, green perovskite, and red QD), $R_{KSF}G_PB$ (blue LED, green perovskite, and red KSF phosphor), and $R_{SLA}G_PB$ (blue LED, green perovskite, and red SLA phosphor). With the two choices of CFs, there will be eight cases in total. The parameters that are

allowed to change are the emission peak wavelengths of blue LED, green perovskite, red LED, and red QD. The fitting parameters of blue and red LEDs are from [110], the SPDs of green perovskite and red QDs are from [99], the SPD of KSF phosphor is from [111], and that of SLA phosphor is from [112]. All of the SPDs are plotted in Figure 10b and the fitting parameters (including $\Delta\lambda$) used in the SP7 model are listed in Table 1.

Implementing the same optimization method described in Section 3.1, Pareto Fronts of all cases are demonstrated in Figure 11a. The solid lines represent the calculated results using CF1, whereas the dashed lines refer to the results with CF2. Due to the intrinsic optical properties of these two CFs, CF2 always provides a wider CGC at the cost of TLE. Interestingly, although the red LED has narrower FWHM than red QD, red QD offers even larger highest-possible CGC. This is because the SPD of red QD is more similar to Gaussian and shows narrower "tails". The "tails" gives rise to larger color crosstalk and ultimately sacrifices CGC. It is worth mentioning that, since the down-converting photon energy is not included in TLE, red LED should be more energy-efficient than red QD in the ideal case. KSF phosphor, on the other hand, presents lower highest-possible CGC, since its SPD is fixed. However, SLA phosphor can compete with red QD and red LED in highest-possible CGC even with fixed SPD. This can be ascribed to its deep-red emission peak wavelength, which accommodates the CFs well. Nevertheless, the broader band of SLA phosphor lowers its TLE noticeably. Details of the optimized results can be found in Table 2.

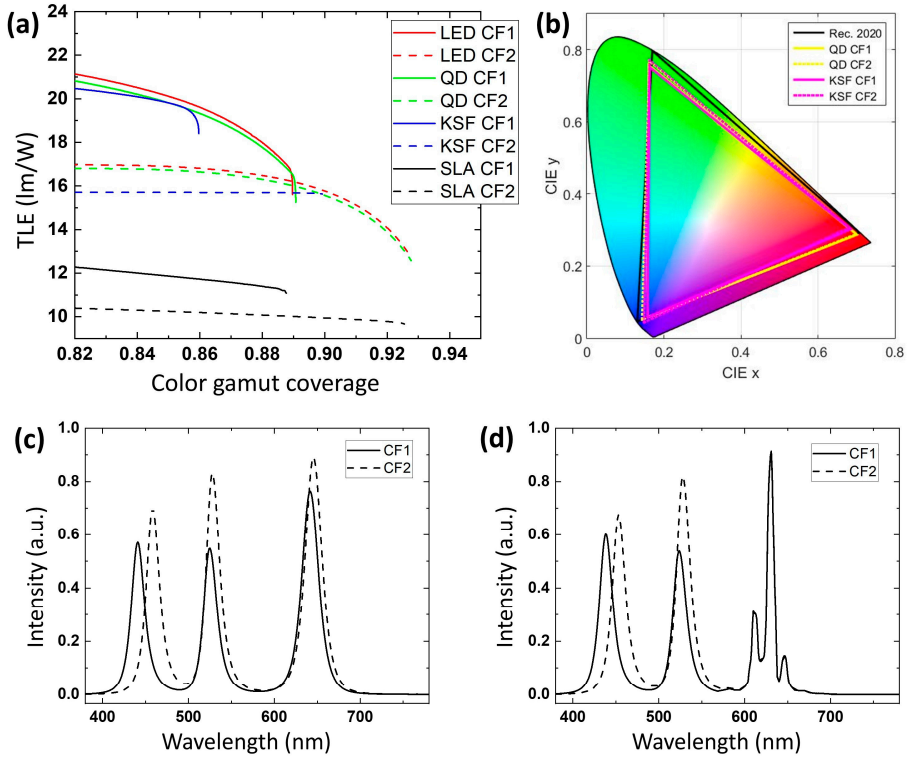

Figure 11. (**a**) *Pareto Fronts* of hybrid-backlight in-plane switching liquid-crystal display (IPS LCDs) with different red emitters and color filters. (**b**) Simulated color gamut for optimized QD- and KSF phosphor-based hybrid LCDs with different color filters. Optimized emission spectra of (**c**) QD- and (**d**) KSF phosphor-based hybrid backlight without any modulation for the two different color filters.

Table 2. Optimized values of wide color-gamut IPS LCDs using different red emitters.

	CF1		CF2	
	CGC	TLE (lm/W)	CGC	TLE (lm/W)
Red LED	89.0%	16.2	92.7%	13.0
Red QD	89.1%	16.1	92.8%	12.6
KSF	86.0%	18.8	89.9%	15.6
SLA	88.8%	11.1	92.6%	9.7

Examples of using emission-tunable red emitter (QD) and fixed phosphor (KSF) are further investigated. Figure 11b depicts the color gamut area of some cases that are summarized in Table 2. The red primary color for QD using both CFs is closer to the primary colors of Rec. 2020 standard compared to the other two primary colors (i.e. green and blue). This is due to the more severe color crosstalk between green and blue CFs. In comparison with QD, KSF phosphor with fixed emission peak wavelength should sacrifice all the primaries more. This can also be sensed from Figure 11c,d, which presents the white backlight without any modulations (by LC, CF, etc.) for the two emitters. To achieve wide color gamut, the emission peak wavelengths of these three colors should be separated far enough according to CFs. For example, for both red emitters, the emission peak wavelengths of green and blue are separated further away using CF1 due to its more severe color crosstalk when comparing to CF2. To accomplish a larger CGC in the future, tailoring the SPD of emitters (especially narrowing the "tails") and redesigning the CFs [109,113–115] will be meaningful.

5. Future Challenges

5.1. Materials Development

So far, very few studies have reported PNCs with relatively good stability against external stresses. Yet, the long-term stability still needs to be tested. Moreover, the current strategy of integrating PNCs into LCD backlight is through on-surface integration. To achieve on-chip configuration, further improvement of thermo- and photo-stability, increased optical density, and tailoring of the form factors are needed. Meanwhile, the state-of-the-art red PNCs still show a wider FWHM than Cd-based QDs. The development of stable and possibly narrower-band red PNCs is highly demanding for non-hybrid configurations. Another intriguing candidate that can boost the efficiency of LCD backlight is the perovskite nanorods (PNRs) [116,117]. By preferentially emitting partially linearly polarized light to pass through the first polarizer, the down-converted light can be less absorbed. However, macroscopic alignment of the PNRs remains challenging [118]. On the other hand, PNCs for SSL applications also confront thermo-stability issue. Unlike LCD backlight, the pumping source in SSL often provides a much higher brightness. Under this circumstance, the photo-stability against intense excitation needs to be investigated.

5.2. Device Integration

For LCD backlight, PNC-embedded films have already been used in consumer products. An example is the PQDCF integrated with blue LED and on-chip KSF phosphor. Very recently, mini-LED LCDs are growing [119]. Although the direct-lit configuration is different from edge-lit, the integration of color conversion materials/films is similar. Another possibility to incorporate PNCs is by introducing patterned PNC-CFs on the top of LCs. However, this method is quite hard, as it requires stable PNCs (especially for red ones), patterning ability, and high optical densities. Besides, future research can also be oriented toward integrating multiple functions in one component. In general, LCD backlight consists of many components (films), such as diffuser sheet, BEF, DBEF, etc. If the on-surface PQDCF offers both down-conversion and good light-diffusing capabilities, the loading of the PNCs, and thus the cost will be decreased [49]. Meanwhile, for SSL, current studies

are still limited in lab. Apart from the instability issue, integration strategy is also an important aspect. For example, to avoid thermo-stability issue of PNCs and glare of blue LED, a remote-downconverter configuration is preferred. However, this configuration will inevitably increase the bulkiness and cost. Thus, this aspect needs to be investigated for further practical SSL applications.

6. Conclusions

We have briefly reviewed the recent advances in perovskite nanocrystals-enhanced SSL and LCDs. The PNCs are favored by both SSL and LCDs, in that they are narrowband and color-tunable. However, to be adopted into these applications, the stability issue still needs further investigation. Besides, lead-free PNCs are also emerging. However, their optical performance and stability are still inferior to those of lead halide PNCs. To evaluate the system performance of SSL enabled by PNCs, we first investigate the fitting-curve effect in optimizations. Through our calculation, the performances of using simple Gaussian fitting and precise fitting are comparable, and the correlations between emission peak wavelengths and objectives for both fitting models are very similar. By further optimizations, we prove that the RY_PG_PB type can fulfill the request for highly efficient, good color-rendering, and human-healthy SSL sources. On the other hand, three configurations of LCD using PNCs as downconverters are evaluated. The LCDs using hybrid PNC-QD or PNC-red LED or PNC-SLA phosphor can achieve larger than 92.5% Rec. 2020 color gamut coverage. Finally, we highlight that better configuration or system performance can be realized through further materials development, and device or function integration remains challenging especially for SSL. As the researches on PNCs are still ongoing and they will attract more attention in the future, we believe that the emerging PNCs hold great promise for promoting the development of next-generation SSL and LCDs.

Author Contributions: Methodology, Z.H.; writing—original draft preparation, Z.H. and C.Z.; writing—review and editing, Z.H., C.Z., Y.D. and S.-T.W.; supervision, Y.D. and S.-T.W.

Funding: This research was funded by Air Force Office of Scientific Research (AFOSR), grant number FA9550-14-1-0279.

Conflicts of Interest: The authors declare no conflict of interest.

References

1. Nakamura, S.; Mukai, T.; Senoh, M. High-power GaN pn junction blue-light-emitting diodes. *Jpn. J. Appl. Phys.* **1991**, *30*, L1998–L2001. [CrossRef]
2. Nakamura, S.; Mukai, T.; Senoh, M. Candela-class high-brightness InGaN/AlGaN double-heterostructure blue-light-emitting diodes. *Appl. Phys. Lett.* **1994**, *64*, 1687–1689. [CrossRef]
3. Nakamura, S. The roles of structural imperfections in InGaN-based blue light-emitting diodes and laser diodes. *Science* **1998**, *281*, 956–961. [CrossRef]
4. Crawford, M.H. LEDs for solid-state lighting: Performance challenges and recent advances. *IEEE J. Sel. Top. Quantum Electron.* **2009**, *15*, 1028–1040. [CrossRef]
5. Schubert, E.F.; Kim, J.K. Solid-state lighting sources getting smart. *Science* **2005**, *308*, 1274–1278. [CrossRef] [PubMed]
6. Pimputkar, S.; Speck, J.S.; DenBaars, S.P.; Nakamura, S. Prospects for LED lighting. *Nat. Photonics* **2009**, *3*, 180–182. [CrossRef]
7. Coltrin, M.E.; Tsao, J.Y.; Ohno, Y. Limits on the maximum attainable efficiency for solid-state lighting. *Proc. SPIE* **2007**, *6841*, 2–13.
8. Taguchi, T. Present status of energy saving technologies and future prospect in white LED lighting. *IEEE J. Trans. Electr. Electron. Eng.* **2008**, *3*, 21–26. [CrossRef]
9. Murphy, T.W. Maximum spectral luminous efficacy of white light. *J. Appl. Phys.* **2012**, *111*, 104909. [CrossRef]
10. Pattison, P.M.; Hansen, M.; Tsao, J.Y. LED lighting efficacy: Status and directions. *C. R. Phys.* **2018**, *19*, 134–145. [CrossRef]
11. Pattison, P.M.; Tsao, J.Y.; Brainard, G.C.; Bugbee, B. LEDs for photons, physiology and food. *Nature* **2018**, *563*, 493–500. [CrossRef] [PubMed]

12. *Parameter Values for the HDTV Standards for Production and International Programme Exchange*; ITU Recommendation BT.709-6; International Telecommunication Union (ITU): Geneva, Switzerland, 2015.
13. *Parameter Values for Ultra-High Definition Television Systems for Production and International Programme Exchange*; ITU Recommendation BT.2020-2; International Telecommunication Union (ITU): Geneva, Switzerland, 2015.
14. Masaoka, K.; Nishida, Y.; Sugawara, M.; Nakasu, E. Design of primaries for a wide-gamut television colorimetry. *IEEE Trans. Broadcast.* **2010**, *56*, 452–457. [CrossRef]
15. Tan, Z.K.; Moghaddam, R.S.; Lai, M.L.; Docampo, P.; Higler, R.; Deschler, F.; Price, M.; Sadhanala, A.; Pazos, L.M.; Credgington, D.; et al. Bright light-emitting diodes based on organometal halide perovskite. *Nat. Nanotechnol.* **2014**, *9*, 687–692. [CrossRef] [PubMed]
16. Lee, M.M.; Teuscher, J.; Miyasaka, T.; Murakami, T.N.; Snaith, H.J. Efficient hybrid solar cells based on mesosuperstructured organometal halide perovskites. *Science* **2012**, *338*, 643–647. [CrossRef] [PubMed]
17. Stranks, S.D.; Snaith, H.J. Metal-halide perovskites for photovoltaic and light-emitting devices. *Nat. Nanotechnol.* **2015**, *10*, 391–402. [CrossRef] [PubMed]
18. Burschka, J.; Pellet, N.; Moon, S.J.; Humphry-Baker, R.; Gao, P.; Nazeeruddin, M.K.; Grä tzel, M. Sequential deposition as a route to high-performance perovskite-sensitized solar cells. *Nature* **2013**, *499*, 316–319. [CrossRef]
19. Saliba, M.; Matsui, T.; Seo, J.Y.; Domanski, K.; Correa-Baena, J.P.; Nazeeruddin, M.K.; Zakeeruddin, S.M.; Tress, W.; Abate, A.; Hagfeldt, A.; et al. Cesium-containing triple cation perovskite solar cells: Improved stability, reproducibility and high efficiency. *Energy Environ. Sci.* **2016**, *9*, 1989–1997. [CrossRef]
20. Liu, Y.; Sun, J.; Yang, Z.; Yang, D.; Ren, X.; Xu, H.; Yang, Z.; Liu, S. 20-mm-Large Single-Crystalline Formamidinium-Perovskite Wafer for Mass Production of Integrated Photodetectors. *Adv. Opt. Mater.* **2016**, *4*, 1829–1837. [CrossRef]
21. Fang, Y.J.; Dong, Q.F.; Shao, Y.C.; Yuan, Y.B.; Huang, J.S. Highly narrowband perovskite single-crystal photodetectors enabled by surface-charge recombination. *Nat. Photonics* **2015**, *9*, 679–686. [CrossRef]
22. Chin, X.Y.; Cortecchia, D.; Yin, J.; Bruno, A.; Soci, C. Lead iodide perovskite light-emitting field-effect transistor. *Nat. Commun.* **2015**, *6*, 7383. [CrossRef]
23. Kojima, A.; Teshima, K.; Shirai, Y.; Miyasaka, T. Organometal Halide Perovskites as Visible-Light Sensitizers for Photovoltaic Cells. *J. Am. Chem. Soc.* **2009**, *131*, 6050–6051. [CrossRef]
24. Snaith, H.J. Perovskites: The Emergence of a New Era for Low-Cost, High-Efficiency Solar Cells. *J. Phys. Chem. Lett.* **2013**, *4*, 3623–3630. [CrossRef]
25. Christians, J.A.; Miranda Herrera, P.A.; Kamat, P.V. Transformation of the excited state and photovoltaic efficiency of $CH_3NH_3PbI_3$ perovskite upon controlled exposure to humidified air. *J. Am. Chem. Soc.* **2015**, *137*, 1530–1538. [CrossRef] [PubMed]
26. Akkerman, Q.A.; Rainò, G.; Kovalenko, M.V.; Manna, L. Genesis, Challenges and Opportunities for Colloidal Lead Halide Perovskite Nanocrystals. *Nat. Mater.* **2018**, *17*, 394–405. [CrossRef] [PubMed]
27. Deschler, F.; Price, M.; Pathak, S.; Klintberg, L.E.; Jarausch, D.D.; Higler, R.; Huttner, S.; Leijtens, T.; Stranks, S.D.; Snaith, H.J.; et al. High photoluminescence efficiency and optically pumped lasing in solution-processed mixed halide perovskite semiconductors. *J. Phys. Chem. Lett.* **2014**, *5*, 1421–1426. [CrossRef]
28. Qian, L.; Zheng, Y.; Xue, J.; Holloway, P.H. Stable and efficient quantum-dot light-emitting diodes based on solution-processed multilayer structures. *Nat. Photonics* **2011**, *5*, 543–548. [CrossRef]
29. Xing, G.; Mathews, N.; Lim, S.S.; Yantara, N.; Liu, X.; Sabba, D.; Gratzel, M.; Mhaisalkar, S.; Sum, T.C. Low-temperature solution-processed wavelength-tunable perovskites for lasing. *Nat. Mater.* **2014**, *13*, 476–480. [CrossRef]
30. Veldhus, S.A.; Boix, P.P.; Yantara, N.; Li, M.; Sum, T.C.; Mathews, N.; Mhaisalkar, S.G. Perovskite materials for light-emitting diodes and lasers. *Adv. Mater.* **2016**, *28*, 6804–6834. [CrossRef]
31. Bai, S.; Yuan, Z.; Gao, F. Colloidal metal halide perovskite nanocrystals: Synthesis, characterization, and applications. *J. Mater. Chem. C* **2016**, *4*, 3898–3904. [CrossRef]
32. Huang, H.; Bodnarchuk, M.I.; Kershaw, S.V.; Kovalenko, M.V.; Rogach, A.L. Lead halide perovskite nanocrystals in the research spotlight: Stability and defect tolerance. *ACS Energy Lett.* **2017**, *2*, 2071–2083. [CrossRef]

33. Protesescu, L.; Yakunin, S.; Bodnarchuk, M.I.; Krieg, F.; Caputo, R.; Hendon, C.H.; Yang, R.X.; Walsh, A.; Kovalenko, M.V. Nanocrystals of Cesium Lead Halide Perovskites ($CsPbX_3$, X = Cl, Br, and I): Novel Optoelectronic Materials Showing Bright Emission with Wide Color Gamut. *Nano Lett.* **2015**, *15*, 3692–3696. [CrossRef] [PubMed]
34. Zhang, F.; Zhong, H.; Chen, C.; Wu, X.G.; Hu, X.; Huang, H.; Han, J.; Zou, B.; Dong, Y. Brightly Luminescent and Color-Tunable Colloidal $CH_3NH_3PbX_3$ (X = Br, I, Cl) Quantum Dots: Potential Alternatives for Display Technology. *ACS Nano* **2015**, *9*, 4533–4542. [CrossRef] [PubMed]
35. Pathak, S.; Sakai, N.; Wisnivesky Rocca Rivarola, F.; Stranks, S.D.; Liu, J.; Eperon, G.E.; Ducati, C.; Wojciechowski, K.; Griffiths, J.T.; Haghighirad, A.A.; et al. Perovskite Crystals for Tunable White Light Emission. *Chem. Mater.* **2015**, *27*, 8066–8075. [CrossRef]
36. Bekenstein, Y.; Koscher, B.A.; Eaton, S.W.; Yang, P.; Alivisatos, A.P. Highly Luminescent Colloidal Nanoplates of Perovskite Cesium Lead Halide and Their Oriented Assemblies. *J. Am. Chem. Soc.* **2015**, *137*, 16008–16011. [CrossRef] [PubMed]
37. Huang, H.; Susha, A.S.; Kershaw, S.V.; Hung, T.F.; Rogach, A.L. Control of Emission Color of High Quantum Yield $CH_3NH_3PbBr_3$ Perovskite Quantum Dots by Precipitation Temperature. *Adv. Sci.* **2015**, *2*, 1–5. [CrossRef] [PubMed]
38. Weidman, M.C.; Seitz, M.; Stranks, S.D.; Tisdale, W.A. Highly Tunable Colloidal Perovskite Nanoplatelets through Variable Cation, Metal, and Halide Composition. *ACS Nano* **2016**, *10*, 7830–7839. [CrossRef]
39. Sutherland, B.R.; Sargent, E.H. Perovskite Photonic Sources. *Nat. Photonics* **2016**, *10*, 295–302. [CrossRef]
40. Levchuk, I.; Osvet, A.; Tang, X.; Brandl, M.; Perea, J.D.; Hoegl, F.; Matt, G.J.; Hock, R.; Batentschuk, M.; Brabec, C.J. Brightly Luminescent and Color-Tunable Formamidinium Lead Halide Perovskite $FAPbX_3$(X = Cl, Br, I) Colloidal Nanocrystals. *Nano Lett.* **2017**, *17*, 2765–2770. [CrossRef]
41. Leijtens, T.; Eperon, G.E.; Noel, N.K.; Habisreutinger, S.N.; Petrozza, A.; Snaith, H.J. Stability of Metal Halide Perovskite Solar Cells. *Adv. Energy Mater.* **2015**, *5*, 1–23. [CrossRef]
42. Niu, G.; Guo, X.; Wang, L. Review of Recent Progress in Chemical Stability of Perovskite Solar Cells. *J. Mater. Chem. A* **2015**, *3*, 8970–8980. [CrossRef]
43. Berhe, T.A.; Su, W.N.; Chen, C.H.; Pan, C.J.; Cheng, J.H.; Chen, H.M.; Tsai, M.C.; Chen, L.Y.; Dubale, A.A.; Hwang, B.J. Organometal Halide Perovskite Solar Cells: Degradation and Stability. *Energy Environ. Sci.* **2016**, *9*, 323–356. [CrossRef]
44. Juarez-Perez, E.J.; Hawash, Z.; Raga, S.R.; Ono, L.K.; Qi, Y. Thermal Degradation of $CH_3NH_3PbI_3$ Perovskite into NH_3 and CH_3I Gases Observed by Coupled Thermogravimetry−Mass Spectrometry Analysis. *Energy Environ. Sci.* **2016**, *9*, 3406–3410. [CrossRef]
45. Conings, B.; Drijkoningen, J.; Gauquelin, N.; Babayigit, A.; D'Haen, J.; D'Olieslaeger, L.; Ethirajan, A.; Verbeeck, J.; Manca, J.; Mosconi, E.; et al. Intrinsic Thermal Instability of Methylammonium Lead Trihalide Perovskite. *Adv. Energy Mater.* **2015**, *5*, 1500477. [CrossRef]
46. Xu, L.; Chen, J.; Song, J.; Li, J.; Xue, J.; Dong, Y.; Cai, B.; Shan, Q.; Han, B.; Zeng, H. Double-Protected All-Inorganic Perovskite Nanocrystals by Crystalline Matrix and Silica for Triple-Modal Anti-Counterfeiting Codes. *ACS Appl. Mater. Interfaces* **2017**, *9*, 26556–26564. [CrossRef] [PubMed]
47. Li, X.; Wang, Y.; Sun, H.; Zeng, H. Amino-Mediated Anchoring Perovskite Quantum Dots for Stable and Low-Threshold Random Lasing. *Adv. Mater.* **2017**, *29*, 1–9. [CrossRef] [PubMed]
48. Li, X.; Zhang, K.; Li, J.; Chen, J.; Wu, Y.; Liu, K.; Song, J.; Zeng, H. Heterogeneous Nucleation toward Polar-Solvent-Free, Fast, and One-Pot Synthesis of Highly Uniform Perovskite Quantum Dots for Wider Color Gamut Display. *Adv. Mater. Interfaces* **2018**, *5*, 1–9. [CrossRef]
49. Wei, Y.; Deng, X.; Xie, Z.; Cai, X.; Liang, S.; Ma, P.; Hou, Z.; Cheng, Z.; Lin, J. Enhancing the Stability of Perovskite Quantum Dots by Encapsulation in Crosslinked Polystyrene Beads via a Swelling–Shrinking Strategy toward Superior Water Resistance. *Adv. Funct. Mater.* **2017**, *27*, 1–8. [CrossRef]
50. Zhang, C.; Zhang, C.; He, J.; Chen, H.; Tan, G.; Zhou, L.; Wu, S. Converting Light Diffusing Polymer Powders into Stable Perovskite- Based Tunable Downconverters. *SID Int. Symp. Dig. Tech. Pap.* **2018**, *49*, 222–224. [CrossRef]
51. Zhou, Q.; Bai, Z.; Lu, W.G.; Wang, Y.; Zou, B.; Zhong, H. In Situ Fabrication of Halide Perovskite Nanocrystal-Embedded Polymer Composite Films with Enhanced Photoluminescence for Display Backlights. *Adv. Mater.* **2016**, *28*, 9163–9168. [CrossRef]

52. Wang, Y.; He, J.; Chen, H.; Chen, J.; Zhu, R.; Ma, P.; Towers, A.; Lin, Y.; Gesquiere, A.J.; Wu, S.T.; et al. Ultrastable, Highly Luminescent Organic–Inorganic Perovskite–Polymer Composite Films. *Adv. Mater.* **2016**, *28*, 10710–10717. [CrossRef]
53. Chang, S.; Bai, Z.; Zhong, H. In Situ Fabricated Perovskite Nanocrystals: A Revolution in Optical Materials. *Adv. Opt. Mater.* **2018**, *6*, 1800380. [CrossRef]
54. Giustino, F.; Snaith, H.J. Toward Lead-Free Perovskite Solar Cells. *ACS Energy Lett.* **2016**, *1*, 1233–1240. [CrossRef]
55. Swarnkar, A.; Ravi, V.K.; Nag, A. Beyond Colloidal Cesium Lead Halide Perovskite Nanocrystals: Analogous Metal Halides and Doping. *ACS Energy Lett.* **2017**, *2*, 1089–1098. [CrossRef]
56. McCall, K.M.; Stoumpos, C.C.; Kostina, S.S.; Kanatzidis, M.G.; Wessels, B.W. Strong Electron−Phonon Coupling and Self- Trapped Excitons in the Defect Halide Perovskites $A_3M_2I_9$ (A = Cs, Rb; M = Bi, Sb). *Chem. Mater.* **2017**, *29*, 4129–4145. [CrossRef]
57. Babayigit, A.; Ethirajan, A.; Muller, M.; Conings, B. Toxicity of organometal halide perovskite solar cells. *Nat. Mater.* **2016**, *15*, 247–251. [CrossRef]
58. Zhou, C.; Tian, Y.; Wang, M.; Rose, A.; Besara, T.; Doyle, N.K.; Yuan, Z.; Wang, J.C.; Clark, R.; Hu, Y.; et al. Low-dimensional organic tin bromide perovskites and their photoinduced structural transformation. *Angew. Chem. Int. Ed.* **2017**, *56*, 9018–9022. [CrossRef]
59. George, N.C.; Denault, K.A.; Seshadri, R. Phosphors for solid-state white lighting. *Annu. Rev. Mater. Res.* **2013**, *43*, 481–501. [CrossRef]
60. Setlur, A.A. Phosphors for LED-based solid-state lighting. *Electrochem. Soc. Interface* **2009**, *18*, 32–36.
61. Li, G.; Tian, Y.; Zhao, Y.; Lin, J. Recent progress in luminescence tuning of Ce 3+ and Eu 2+-activated phosphors for pc-WLEDs. *Chem. Soc. Rev.* **2015**, *44*, 8688–8713. [CrossRef]
62. Shimizu, K.T.; Böhmer, M.; Estrada, D.; Gangwal, S.; Grabowski, S.; Bechtel, H.; Kang, E.; Vampola, K.J.; Chamberlin, D.; Shchekin, O.B.; et al. Toward commercial realization of quantum dot based white light-emitting diodes for general illumination. *Photonics Res.* **2017**, *5*, A1–A6. [CrossRef]
63. Mangum, B.D.; Landes, T.S.; Theobald, B.R.; Kurtin, J.N. Exploring the bounds of narrow-band quantum dot downconverted LEDs. *Photonics Res.* **2017**, *5*, A13–A22. [CrossRef]
64. Li, X.; Wu, Y.; Zhang, S.; Cai, B.; Gu, Y.; Song, J.; Zeng, H. CsPbX3 quantum dots for lighting and displays: Room-temperature synthesis, photoluminescence superiorities, underlying origins and white light-emitting diodes. *Adv. Funct. Mater.* **2016**, *26*, 2435–2445. [CrossRef]
65. Chen, D.; Fang, G.; Chen, X. Silica-Coated Mn-Doped $CsPb(Cl/Br)_3$ Inorganic Perovskite Quantum Dots: Exciton-to-Mn Energy Transfer and Blue-Excitable Solid-State Lighting. *ACS Appl. Mater. Interfaces* **2017**, *9*, 40477–40487. [CrossRef] [PubMed]
66. Yoon, H.C.; Oh, J.H.; Lee, S.; Park, J.B.; Do, Y.R. Circadian-tunable perovskite quantum dot-based down-converted multi-package white LED with a color fidelity index over 90. *Sci. Rep.* **2017**, *7*, 2808. [CrossRef] [PubMed]
67. Yoon, H.C.; Kang, H.; Lee, S.; Oh, J.H.; Yang, H.; Do, Y.R. Study of perovskite QD down-converted LEDs and six-color white LEDs for future displays with excellent color performance. *ACS Appl. Mater. Interfaces* **2016**, *8*, 18189–18200. [CrossRef] [PubMed]
68. Schubert, E.F.; Gessmann, T.; Kim, J.K. *Light Emitting Diodes*; Wiley: New York, NY, USA, 2005.
69. Žukauskas, A.; Vaicekauskas, R.; Ivanauskas, F.; Gaska, R.; Shur, M.S. Optimization of white polychromatic semiconductor lamps. *Appl. Phys. Lett.* **2002**, *80*, 234–236. [CrossRef]
70. Žukauskas, A.; Vaicekauskas, R.; Ivanauskas, F.; Vaitkevičius, H.; Shur, M.S. Spectral optimization of phosphor-conversion light-emitting diodes for ultimate color rendering. *Appl. Phys. Lett.* **2008**, *93*, 051115. [CrossRef]
71. He, G.; Yan, H. Optimal spectra of the phosphor-coated white LEDs with excellent color rendering property and high luminous efficacy of radiation. *Opt. Express* **2011**, *19*, 2519–2529. [CrossRef] [PubMed]
72. Luo, Z.; Chen, H.; Liu, Y.; Xu, S.; Wu, S.T. Color-tunable light emitting diodes based on quantum dot suspension. *Appl. Opt.* **2015**, *54*, 2845–2850. [CrossRef]
73. Dai, Q.; Hao, L.; Lin, Y.; Cui, Z. Spectral optimization simulation of white light based on the photopic eyesensitivity curve. *J. Appl. Phys.* **2016**, *119*, 053103. [CrossRef]
74. He, Z.; Chen, H.; Lee, Y.H.; Wu, S.T. Tuning the correlated color temperature of white light-emitting diodes resembling Planckian locus. *Opt. Express* **2018**, *26*, A136–A143. [CrossRef]

75. Pauley, S.M. Lighting for the human circadian clock: Recent research indicates that lighting has become a public health issue. *Med. Hypotheses* **2004**, *63*, 588–596. [CrossRef]
76. Anderson, J.L.; Glod, C.A.; Dai, J.; Lockley, S.W. Lux vs. wavelength in light treatment of seasonal affective disorder. *Acta Psychiatr. Scand.* **2009**, *120*, 203–212. [CrossRef]
77. Gooley, J.J. Treatment of circadian rhythm sleep disorders with light. *Ann. Acad. Med.* **2008**, *37*, 669–676.
78. Boivin, D.B.; Duffy, J.F.; Kronauer, R.E.; Czeisler, C.A. Dose–response relationships for resetting of human circadian color by light. *Nature* **1996**, *379*, 540–542. [CrossRef]
79. Falchi, F.; Cinzano, P.; Elvidge, C.D.; Keith, D.M.; Haim, A.L. Limiting the impact of light pollution on human health, environment and stellar visibility. *J. Environ. Manag.* **2011**, *92*, 2714–2722. [CrossRef]
80. Oh, J.H.; Yang, S.J.; Do, Y.R. Healthy, natural, efficient and tunable lighting: Four-package white LEDs for optimizing the circadian effect, color quality and vision performance. *Light Sci. Appl.* **2014**, *3*, e141. [CrossRef]
81. Dai, Q.; Shan, Q.; Lam, H.; Hao, L.; Lin, Y.; Cui, Z. Circadian-effect engineering of solid-state lighting spectra for beneficial and tunable lighting. *Opt. Express* **2016**, *24*, 20049–20058. [CrossRef]
82. Žukauskas, A.; Vaicekauskas, R. Tunability of the circadian action of tetrachromatic solid-state light sources. *Appl. Phys. Lett.* **2015**, *106*, 041107. [CrossRef]
83. Zheng, L.; Wu, T.; Lu, Y.; Gao, Y.; Wang, Y.; Zhu, L.; Guo, Z.; Chen, Z. Spectral optimization of threeprimary LEDs by considering the circadian action factor. *IEEE Photonics J.* **2016**, *8*, 8200209. [CrossRef]
84. Berson, D.M.; Dunn, F.A.; Takao, M. Phototransduction by retinal ganglion cells that set the circadian clock. *Science* **2002**, *295*, 1070–1073. [CrossRef]
85. Gall, D. Circadiane Lichtgrößen und deren messtechnische ermittlung. *Licht* **2002**, *54*, 1292–1297.
86. Gall, D.; Beiske, K. Definition and measurement of circadian radiometric quantities. In Proceedings of the 2004 CIE Symposium on Light and Health: Non-visual Effects (Commission Internationale de l'E´ clairage, 2004), Vienna, Austria, 30 September–2 October 2004; pp. 129–132.
87. Ohno, Y. Spectral design considerations for color rendering of white LED light sources. *Opt. Eng.* **2005**, *44*, 111302. [CrossRef]
88. Davis, W.; Ohno, Y. Color quality scale. *Opt. Eng.* **2010**, *49*, 033602. [CrossRef]
89. Coello, C.A.C.; Lamont, G.B. *Applications of Multi-Objective Evolutionary Algorithms*; World Scientific: Singapore, 2004.
90. Žukauskas, A.; Vaicekauskas, R.; Vitta, P.; Zabiliūtė, A.; Petrulis, A.; Shur, M. Color rendition engineering of phosphor-converted light-emitting diodes. *Opt. Express* **2013**, *21*, 26642–26656. [CrossRef]
91. He, G.; Tang, J. Spectral optimization of color temperature tunable white LEDs with excellent color rendering and luminous efficacy. *Opt. Lett.* **2014**, *39*, 5570–5573. [CrossRef]
92. Chien, M.C.; Tien, C.H. Multispectral mixing scheme for LED clusters with extended operational temperature window. *Opt. Express* **2012**, *20*, A245–A254. [CrossRef]
93. Guo, Z.; Lu, H.; Shih, T.; Lin, Y.; Lu, Y.; Chen, Z. Spectral optimization of candle-like white light-emitting diodes with high color rendering index and luminous efficacy. *J. Disp. Technol.* **2016**, *12*, 1393–1397. [CrossRef]
94. Okumura, T.; Tagaya, A.; Koike, Y.; Horiguchi, M.; Suzuki, H. Highly-efficient backlight for liquid crystal display having no optical films. *Appl. Phys. Lett.* **2003**, *83*, 2515–2517. [CrossRef]
95. Käläntär, K. Modified functional light-guide plate for backlighting transmissive LCDs. *J. Soc. Inf. Disp.* **2003**, *11*, 641–645. [CrossRef]
96. Feng, D.; Yan, Y.; Yang, X.; Jin, G.; Fan, S. Novel integrated lightguide plates for liquid crystal display backlight. *J. Opt. A Pure Appl. Opt.* **2005**, *7*, 111–117. [CrossRef]
97. Anandam, M. Progress of LED backlights for LCDs. *J. Soc. Inf. Disp.* **2008**, *16*, 287–310. [CrossRef]
98. Huang, H.T.; Huang, Y.P.; Tsai, C.C. Planar lighting system using array of blue LEDs to excite yellow remote phosphor film. *J. Disp. Technol.* **2011**, *7*, 44–51. [CrossRef]
99. He, J.; Chen, H.; Chen, H.; Wang, Y.; Wu, S.T.; Dong, Y. Hybrid downconverters with green perovskite-polymer composite films for wide color gamut displays. *Opt. Express* **2017**, *25*, 12915–12925. [CrossRef]
100. Chen, J.; Hardev, V.; Hartlove, J.; Hofler, J.; Lee, E. A high-efficiency wide-color-gamut solid-state backlight system for LCDs using quantum dot enhancement film. *Proc. SID Symp. Dig. Tech. Papers* **2012**, *43*, 895–896. [CrossRef]

101. Chen, H.; He, J.; Wu, S.T. Recent advances on quantum-dot-enhanced liquid crystal displays. *IEEE J. Sel. Top. Quantum Electron.* **2017**, *23*, 1900611. [CrossRef]
102. Xie, R.J.; Kimoto, K.; Sekiguchi, T.; Yamamoto, Y.; Suehiro, T.; Mitomo, M.; Hirosaki, N. Characterization and properties of green-emitting β-SiAlON:Eu2+ powder phosphors for white light-emitting diodes. *Appl. Phys. Lett.* **2005**, *86*, 211905.
103. Li, S.; Xie, R.J.; Takeda, T.; Hirosaki, N. Critical Review—Narrow-Band Nitride Phosphors for Wide Color-Gamut White LED Backlighting. *ECS J. Solid State Sci. Technol.* **2018**, *7*, R3064–R3078. [CrossRef]
104. Harbers, G.; Hoelen, C. High performance LCD backlighting using high intensity red, green and blue light emitting diodes. *Proc. SID Symp. Dig. Tech. Pap.* **2001**, *32*, 702–705. [CrossRef]
105. Folkerts, W. LED backlighting concepts with high flux LEDs. *Proc. SID Symp. Dig. Tech. Pap.* **2004**, *35*, 1226–1229. [CrossRef]
106. Lu, R.B.; Gauza, S.; Wu, S.T. LED-lit LCD TVs. *Mol. Cryst. Liq. Cryst.* **2008**, *488*, 246–259. [CrossRef]
107. Luo, Z.; Chen, Y.; Wu, S.T. Wide color gamut LCD with a quantum dot backlight. *Opt. Express* **2013**, *21*, 26269–26284. [CrossRef]
108. Luo, Z.; Xu, D.; Wu, S.T. Emerging quantum-dots-enhanced LCDs. *J. Disp. Technol.* **2014**, *10*, 526–539. [CrossRef]
109. Zhu, R.; Luo, Z.; Chen, H.; Dong, Y.; Wu, S.T. Realizing Rec. 2020 color gamut with quantum dot displays. *Opt. Express* **2015**, *23*, 23680–23693. [CrossRef]
110. Guo, Z.; Liu, K.; Zheng, L.; Shih, T.; Lu, Y.; Wu, T.; Lin, Y.; Zhang, X.; Zheng, J.; Chen, J.; et al. Investigation on three-hump phosphor-coated white light-emitting diodes for healthy lighting by genetic algorithm. *IEEE Photonics J.* **2018**, *11*, 8200110. [CrossRef]
111. Wang, L.; Wang, X.; Kohsei, T.; Yoshimura, K.; Izumi, M.; Hirosaki, N.; Xie, R.J. Highly efficient narrowband green and red phosphors enabling wider color-gamut LED backlight for more brilliant displays. *Opt. Express* **2015**, *23*, 28707–28717. [CrossRef]
112. Pust, P.; Weiler, V.; Hecht, C.; Tücks, A.; Wochnik, A.S.; Henß, A.K.; Wiechert, D.; Scheu, C.; Schmidt, P.J.; Schnick, W. Narrow-band red-emitting Sr[LiAl3N4]:Eu2+ as a next-generation LED-phosphor material. *Nat. Mater.* **2014**, *13*, 891–896. [CrossRef]
113. Chen, H.; Zhu, R.; Tan, G.; Li, M.C.; Lee, S.L.; Wu, S.T. Enlarging the color gamut of liquid crystal displays with a functional reflective polarizer. *Opt. Express* **2017**, *25*, 102–111. [CrossRef]
114. Chen, H.; Zhu, R.; He, J.; Duan, W.; Hu, W.; Lu, Y.Q.; Li, M.C.; Lee, S.L.; Dong, Y.; Wu, S.T. Going beyond the limit of an LCD's color gamut. *Light-Sci. Appl.* **2017**, *6*, e17043. [CrossRef]
115. Chen, H.; Lee, J.H.; Lin, B.Y.; Chen, S.; Wu, S.T. Liquid crystal display and organic light-emitting diode display: Present status and future perspectives. *Light-Sci. Appl.* **2018**, *7*, 17168. [CrossRef]
116. Urban, J.J.; Yun, W.S.; Gu, Q.; Park, H. Synthesis of single-crystalline perovskite nanorods composed of barium titanate and strontium titanate. *J. Am. Chem. Soc.* **2002**, *124*, 1186–1187. [CrossRef]
117. Aharon, S.; Etgar, L. Two dimensional organometal halide perovskite nanorods with tunable optical properties. *Nano Lett.* **2016**, *16*, 3230–3235. [CrossRef]
118. He, J.; Towers, A.; Wang, Y.; Yuan, P.; Zhang, J.; Chen, J.; Gesquiere, A.J.; Wu, S.T.; Dong, Y. In-situ synthesis and macroscale alignment of CsPbBr3 Perovskite nanorods in polymer matrix. *Nanoscale* **2018**, *10*, 15436–15441. [CrossRef]
119. Tan, G.; Huang, Y.; Li, M.C.; Lee, S.L.; Wu, S.T. High dynamic range liquid crystal displays with a mini-LED backlight. *Opt. Express* **2018**, *26*, 16572–16584. [CrossRef]